High-Modulus Homochiral Torsional Oxide Ceramic Artificial Muscles

Jianhua Yan (✉ yanjianhua@dhu.edu.cn)

Donghua University

jiawei wu

https://orcid.org/0000-0001-6781-3581

Chuang Zhu

Donghua University

Yongshi Guo

Donghua University

Jiangtao Di

Suzhou Institute of Nano-Tech and Nano-Bionics, Chinese Academy of Sciences

Xiaohua Zhang

Donghua University

Liying Wei

Donghua University

Xuwang Tian

Jilin University

Kun Fu

University of Delaware

Article

Additional Declarations: There is **NO** Competing Interest.

Abstract

Artificial muscles are soft actuators used to mimic human muscle movements, but using oxide ceramics to fabricate high-modulus artificial muscles is a challenge since they are prone to fracture during homochiral torsion. Here, we report a strategy of ceramic metallization to solve the problem of low-shear and low-stretchability of ceramics and fabricate homochiral coiled alumina yarn artificial muscles with a solenoid structure. The alumina muscle can carry objects of 0.28 million times its own weight and provide a high actuation stress of 483.5 MPa while maintaining a large tensile stroke of 13.5%. In addition, it shows a contraction power 18 times and an energy density 240 times of human muscles, as well as a high energy conversion efficiency of 7.59% under an electric drive mode, which far exceed most reported polymer and carbon muscles. This work realizes large-scale fabrication of high-modulus ceramic muscles.

Introduction

Cheetahs is a mammal with ultra-high explosive power that comes from the coordinated contraction of skeletal muscles under nerve control.[1, 2] This precise dynamic response function relies on the complex hierarchical structures of muscle fibers and their composition material of myosin.[3, 4] Myosin is a kind of Motor protein with DNA supercoiled and solenoid topology structures, the conversion of these two structures cause myosin to move, thereby promoting the movement of living organisms from micro to macro levels.[5, 6] Inspired by skeletal muscles, fiber-based artificial muscles have developed rapidly in the field of soft robots.[7] Polymer yarn is commonly used for preparing artificial muscle since it can easily form a solenoid topology with driving performance through twisting.[8, 9] Unfortunately, the low modulus and tensile strength of polymer yarn muscles limit their applications in micro-robotics that need low actuation stress.[10, 11] In recent years, carbon fiber/nanotube yarns have attracted much attention due to their high modulus and tensile strength.[12, 13] However, it is difficult to achieve high modulus of carbon nanotube filaments formed by the end-to-end connection of short carbon nanotubes, and most of the reported carbon-based artificial muscles still have problems such as poor energy conversion efficiency, low actuation stress, power, and energy density.[14, 15]

As an alternative solution, oxide ceramic filaments have high modulus, high-temperature resistance, and corrosion resistance, which are expected to break through the performance and application bottlenecks of existing artificial muscles.[16, 17] Currently, there is no report of ceramic artificial muscles, mainly limited by the low-shear resistance and poor tensile property of oxide ceramic filaments.[18, 19] Ceramic filaments are prone to breakage during twisting and cannot form a solenoid structure with driving performance.[20, 21] The formation of the solenoid structure is mainly based on the Poynting effect, which is a coupling effect between axial shear deformation and normal tensile strain.[22, 23] This coupling effect usually occurs on polymer yarns and carbon fiber/nanotube yarns, as the boundary condition for its occurrence is usually that the tensile strain of the fibers is > 10%.[24, 25] Oxide ceramic filaments have high modulus at the GPa level, but their almost non-stretchable and non-shear property make it difficult to form a solenoid

structure.[26, 27] In addition, even if the twisting property of oxide ceramic filament is improved under the help of guests, according to the classical theory of Kirchhoff Love, the huge torque energy generated by high modulus materials during twisting will cause the ceramic filament yarn to form a DNA supercoiled structure with low driving performance.[28, 29]

Here, we propose a strategy of ceramic metallization in combination with viscous flow field to improve the shear resistance and tensile strain of oxide ceramic filament yarns for the fabrication of high-modulus coiled Al_2O_3 yarn muscles. First, high modulus and shear-resistant $Cu@Al_2O_3$ yarns were produced on a large scale with a dopamine assisted chemical plating method followed by sintering and rapid annealing under pressurized argon. During this process, the decomposition of dopamine into carbides improved the wettability of Cu/Al_2O_3 interface, and the mutual annexation of crystalline Cu left a dense Cu coating. The Cu layer in contact with the dopamine coating was easily oxidized to CuO, which formed a eutectic liquid surface with Cu during the sintering, and then reacted with Al_2O_3 to form a bonding layer. The bonding interface and Cu coating significantly enhanced the shear resistance of the yarn. Then, the strain of $Cu@Al_2O_3$ yarn was greatly enhanced by immersing it into viscous paraffin and thus could construct coiled structures by over-twisting. As a result, this ceramic artificial muscle showed a high tensile stroke of 13.5%, a high actuation stress of 483.5 MPa, and a large energy density of 9.8 J/g. Under an electric drive, it generated a high energy conversion efficiency of 7.59%, and an output power of 10.3 W which was 18 times of the human muscle contraction power.

Results

Large-scale fabrication of Al_2O_3 filament yarn muscles with solenoid structures

The Al_2O_3 filament yarns fabricated with a centrifugal spinning technique showed a high modulus of ~ 130 GPa, but a low shear resistance. After metallization treatment, the $Cu@Al_2O_3$ filament had a high modulus of ~ 180 GPa and great twistability. The large-scale fabrication process is shown in Fig. 1a, after being led out of the winding drum, the Al_2O_3 filament yarn passed through a dopamine solution and a chemical plating solution in turn. Dopamine was an adhesive that could provide strong adhesion of Cu and Al_2O_3, thus a uniform nano-Cu layer could grow on the Al_2O_3 filaments at room temperature. The initial plated thin Cu layer in contact with dopamine easily became CuO due to the existence of active oxygen in the plating solution. Then, the composite filaments were sequentially sintered at 300°C and 900°C in an inert atmosphere followed by rapid annealing to obtain high-modulus $Cu@Al_2O_3$ filaments.

During this sintering, the dopamine was firstly converted into carbides at 300°C which improved the wettability of Al_2O_3 to Cu. Then at 900°C, Cu and CuO formed a eutectic liquid phase, which could react with Al_2O_3 to form tightly bonded interfaces by producing lattice distortion. Simultaneously, Cu grains started to grow and annex each other, and a densified Cu layer was formed after annealing. The proposed

method is scalable, and the as-prepared rolls of Cu@Al$_2$O$_3$ filament yarns are shown in Fig. 1b, which exhibited metallic luster with high electrical conductivity and torsional property. When the filament was torsional deformed, the huge stress was usually concentrated on the filament surface, and the coated Cu layer served as a lubricant to evenly transmit the torque stress between fibers (Fig. 1c). The twisted Cu@Al$_2$O$_3$ filaments formed an Archimedean helix, and multi-stranded Archimedean spiral yarns were obtained by homochiral twisting several strands of the twisted yarn. As a comparison, the bare Al$_2$O$_3$ filament yarn was easily fractured during twisting.

Despite its high shear resistance, the Cu@Al$_2$O$_3$ filament yarn showed a low tensile strain, which tended to form a DNA supercoiled structure when being over-twisted according to the theory of Kirchhoff Love. Therefore, a viscous flow field of paraffin was introduced to prepare homochiral solenoid topology structures. The viscous paraffin could resist tensile deformation. The magnitude of the viscous force can be expressed by the following formula:

$$F = \eta S \left(\frac{\mathrm{dv}}{\mathrm{dx}} \right)$$

where η is the viscosity coefficient of the fluid, S is the contact area, and $\frac{\mathrm{dv}}{\mathrm{dx}}$ is the velocity gradient. The auxiliary role of the viscous flow field was important to control the transformation of the filament yarn's topology, and the Cu@Al$_2$O$_3$ filament yarn could form a solenoid structure when it was overtwisted under a viscous flow field. The topology changes of the overtwisted Cu@Al$_2$O$_3$ filament yarn required more torque energy due to the presence of a viscous flow field, which promoted to form an intermediate state of solenoid structures (Fig. 1d). The solenoid topology was a transition state that could spontaneously shift toward a DNA supercoiled structure when the viscosity decreased (**Video S1**). The coiled Cu@Al$_2$O$_3$ muscle underwent both the volume actuation of expansion and the structural actuation of topological transformation when it was electrically or thermally stimulated, showing a different actuation system compared with other artificial muscles (Fig. 1e). In addition, the superior high toughness of the Cu@Al$_2$O$_3$ yarn enabled the homochiral coiled muscles with much higher actuation stress, power, and energy densities than polymer muscles, demonstrating great application prospects in the field of soft robotics that require high stress and power/energy densities (Fig. 1f).

Materials characterization

The high modulus Al$_2$O$_3$ yarn can carry a dumbbell or a barbell weighing 0.28 million times its weight (Fig. 2a). The yarn with a α-Al$_2$O$_3$ crystal structure had a high melting point of 2054°C and thus could withstand fire for a long time (**Fig. S1**). The robust and fire-resistant Al$_2$O$_3$ yarn was smooth (Fig. 2b). Dopamine was chosen as the chemical adhesive on the yarn for the subsequent catalyst (Pd^{2+}) capture and Cu plating. The self-polymerization of dopamine was important, and it determined the quality of the plated Cu layer. Here, polyethyleneimine (PEI) was introduced to improve the self-polymerization process, and simultaneously causing the copolymer solution to exhibit color change (**Fig. S2**). The adhesion of

dopamine to Al_2O_3 originated from the o-quinone group formed by the catechol hydroxyl oxidation, which was a transitional functional group in the self-polymerization of dopamine. The ultraviolet spectra were used to characterize the changes in the spontaneous polymerization process of the copolymer, and the o-quinone was located at 350 nm (**Fig. S3a-b**). The PEI promoted to form o-quinone groups and the dopaquinone reached the maximum amount after 6 h, at which point the Al_2O_3 yarn became light yellow with adhesion for the following plating (**Fig. S3c**). The new peaks at 1250 nm and 3250 nm in the Fourier transform infrared (FTIR) spectra confirmed the dopamine and PEI on the yarn (**Fig. S4**). The trace amounts of carbon in the energy dispersive spectroscopy (EDS) also indicated the adhesion of dopamine to the yarn (**Fig. S5a-b**). From the scanning electron microscopy (SEM) images, the yarn did not change much (**Fig. S5c-d**), since the coated dopamine layer was thin, which had a maximum thickness of ~ 60 nm, an arithmetic mean thickness of ~ 24.1 nm, and a root mean square thickness of ~ 30.7 nm (**Fig. S6**).

Furthermore, the Raman spectra showed that the carbon material (dopamine) on the Al_2O_3 filament had a large defect, which was beneficial for capturing Pd^{2+}-ions by catechol hydroxyl (**Fig. S7**). After immersing the Al_2O_3 filament yarns in Pd^{2+} solution for 2 h, lots of Pd^{2+}-ions were captured by dopamine to form catalytic sites. From the X-ray photoelectron spectroscopy (XPS), a small portion of Pd^{2+} were reduced to Pd by dopamine (**Fig. S8a**). Additionally, the XPS showed a decrease in peak intensity of Al with the dopamine coating (**Fig. S8b**). The Al_2O_3 yarns containing the catalytic sites were then immersed in the chemical solution for firmly growing Cu particles. The quality of Cu layer was controlled by adjusting the reaction rate and plating time. A fast reaction rate would cause an overlapping growth of Cu (**Fig. S9a-b**), while a long plating time would cause bloated Cu layer (**Fig. S9c-d**). The X-ray diffraction (XRD) patterns showed that the peaks of Cu and Al_2O_3 coincided at ~ 43°, so the growth of Cu could be observed by comparing the peak intensity (**Fig. S10a**). With increasing time, the (111) peak of Cu showed an upward trend. When the plating time reached 40 min, the peak intensity of Cu was higher than Al_2O_3, indicating that Cu layer had been bloated. The optimal plating time and rate were set as 15 min and ~ $1.0 \cdot 10^{-3}$ g/min (**Fig. S10b**). As shown in Fig. 2c, the dispersed Cu spheres on the yarn was beneficial for removing dopamine under high-temperature sintering.

The sintering temperature for the yarns should be above the decomposition temperature of dopamine and below the melting point of Cu at 1084 °C. The decomposition temperature of dopamine was tested by thermogravimetric (TG) analysis in air, as shown in **Fig. S11**. There were three critical temperature points (180 °C, 240 °C and 800 °C) at which the mass of the yarns decreased rapidly. The former two points corresponded to the transformation of dopamine to carbide, and the latter indicated that carbide was decomposed at 800 °C. Therefore, the sintering temperature was firstly set at 300 °C for 1 h, then at 900 °C for half an hour, and finally quickly annealed. The morphology of Cu after sintering changed from dispersed spheres to densely packed cube crystals, and the diameter of the Cu@Al_2O_3 yarn was reduced (Fig. 2d). From the cross-sectional images, the thickness of the plated Cu layer was ~ 1 μm (**Fig. S12**). Here, sintering temperatures of 500°C and 700 °C were used as controls, and the dispersed Cu spheres also transformed into cube crystals, indicating that Cu already crystallized at 500 °C (**Fig. S13**). However,

these Cu crystals showed different interactions with Al_2O_3 after being treated by different temperatures. As checked by XRD in Fig. 2e, in comparison with the sample that sintered at 500 ℃, the diffraction peak of the sample sintered at 900 ℃ deviated by 0.225° toward height angles, suggesting that Cu interacted with Al_2O_3 more intensively. By contrast, this phenomenon did not occur for the bare Al_2O_3 filament yarns (**Fig. S14**).

Furthermore, the sizes and micro-strains of Cu grains were estimated with the Williamson-Hall method. The Cu grains increased with the plating time and sintering temperatures (Fig. 2f), and the internal stress of the Cu crystals before and after sintering were opposite (**Fig. S15**). The reason was that the growth of Cu during the chemical plating produced outward internal stress, while the high temperature sintering forced Cu to densify inwardly. The Cu@Al_2O_3 filament yarns should not be sintered for a long time at high temperatures, otherwise would form undesired Cu structures. The XPS spectra showed that the densified Cu layer on the Cu@Al_2O_3 yarn was composed of metallic Cu and a small portion of Cu^{2+} and CuO (Fig. 2g). On the contrast, the Cu layer contained a larger portion of Cu^{2+} and CuO before sintering (**Fig. S16**). The EDS spectra of the Cu@Al_2O_3 yarns confirmed that the densified crystals were mainly metallic Cu (**Fig. S17**). From the transmission electron microscopy (TEM), a large area of lattice distortion could be clearly observed at the interface of Cu-Al_2O_3. Before sintering, the lattice spacing of the (110) facet in Al_2O_3 was 0.237 nm, and the lattice spacing of the (111) facet in Cu was 0.208 nm. After being sintered at 900 ℃, a transition layer appeared between Cu and Al_2O_3, while the lattice spacing of Al_2O_3 decreased to 0.230 nm, and the lattice spacing of Cu increased to 0.218 nm (**Fig. S18**). The width of the lattice distortion area was ~ 15nm, and all the amorphous Cu were transformed into crystalline structures (**Fig. S19**).

Dynamic polarization testing was explored to evaluate the densification degree of Cu on the yarns (**Fig. S20a**). Taking the Cu@Al_2O_3 yarn without being sintered as a reference, the relative porosity of the Cu@Al_2O_3-900 ℃ yarn decreased by ~ 15.8%, and the corrosion current intensity increased by 171% (**Fig. S20b**). The enhancement of corrosion current intensity originated from the decrease in polarization resistance, reflecting a significant increase in the densification degree of Cu layers, which could form a continuous conductive path on the yarn (Fig. 2h). On the other hand, the electrochemical impedance spectra (EIS) also confirmed the densification of Cu (Fig. 2i). The equivalent circuit contained the polarization resistance (R_{ct}) of the yarn electrode, which was connected in parallel with the constant phase angle CPE, and then connected in series with the solution internal resistance (R_s). The CPE-P of the yarn was larger than 0.5 (**Fig. S21**), indicating that the yarn electrode behaved as a Warburg impedance, and the yarn was smooth. Therefore, the densified Cu layer gave the Cu@Al_2O_3 filament yarn a stable conductivity that increased linearly with length (Fig. 2j).

Mechanical and electrical properties of homochiral torsional yarns

The Cu@Al_2O_3 yarn sintered at 900 °C exhibited great flexibility and could be arbitrarily knotted (**Fig. S22**). Of note, the bare Al_2O_3 filament yarn could not be twisted because it could not withstand the concentrated torsional stress, while the Cu@Al_2O_3 yarn could withstand the torsional stress due to the ductility of Cu. The simulated distribution of torsional stress in the twisted yarn is shown in Fig. 3a, from which the torsional stress was mainly concentrated on the surface. The method for forming the homochiral ply yarn is shown in Fig. 3b. A single yarn can be twisted into S-type or Z-type structure, and a hierarchical structure can be obtained when twisting two or more ply yarns. For example, a homochiral hierarchical structure can be obtained by twisting two S-twisted yarns into S-type, otherwise a heterochiral hierarchical structure can be obtained by twisting two S-twisted yarns into Z-type. The homochirality of ply yarns can further enhance the torque energy, while the heterochiral structure can balance the torque of the yarn to obtain a stable solenoid structure.

Figure 3c shows the as-fabricated 2-ply, 4-ply, and 8-ply filament yarns with a homochiral solenoid structure. The Cu@Al_2O_3 filament yarn could form different topologies by twisting, and an Archimedean spiral structure was formed when the twisted equilibrium point was at the endpoint. To test the mechanical property, it needs to fix the two ends of the yarns to maintain the stability of the coiled topology. As shown in Fig. 3d, both the coated Cu layer and the homochiral Archimedean structure increased the strength and strain of the yarns. Compared with the bare Al_2O_3 yarn with a tensile strength of 1.045 GPa and a strain of 1.13%, the Cu@Al_2O_3 yarn showed a much higher strength of 2.172 GPa and a high strain of 1.35%. As the number of strands increased, there was a significant increase in strength and strain. For example, the twisted 8-ply yarn exhibited a high strength of 3.9 GPa and a large strain of 2.35%. In addition, the modulus of the Cu@Al_2O_3 yarn was increased from 130 GPa of the bare Al_2O_3 yarn to 180 GPa (Fig. 3e). It is worth to note that the homochiral Archimedean structure by twisting multiple strands of yarns together had no effect on the yarn modulus, but it significantly increased the fracture toughness of the 8-ply yarn from 708 J/m^3 to 4832 J/m^3 (**Fig. S23**).

Next, two typical methods were referred to test the bending stiffness of the yarns. The first one was to measure the bending stiffness B by calculating the deformation of the yarn after hanging a heavy object, and the second one was to obtain the equivalent flexural modulus Eb by calculating the bending diameter of the yarn under a pressure (**Supplementary Methods** and **Fig. S24**). As shown in Fig. 3f, the bending stiffness of the yarn always decreased with the increase of external work and the number of plies. However, the bending stiffness of the 8-ply homochiral torsional yarn increased abnormally to $19.66*10^{-5}$ cN/cm^2. The torsional property of yarns was obtained by using a torsional pendulum method (**Supplementary Methods**), which was based on the balance of mass moment of inertia and angular momentum when the yarn with heavy objects was suspended during rotation. As shown in **Fig. S25**, the single S-twisted (5 turns) Cu@Al_2O_3 yarn exhibited the strongest torsional property. After the twisted single yarn was released, it could recover to the untwisted state and then spontaneously twisted into a ~ 13 turns of Z-type coiled structure, showing a maximum angle change of ~ 360%, confirming the high power of the coiled ceramic yarn. Similar phenomena were observed for the 8-ply yarns, but the homochiral Archimedean structure significantly increased the torsional acceleration of the strands since

the structure would produce frictional energy consumption during torsion, so that the 8-ply yarn could recover to 0° in the shortest time.

Actuation performance of homochiral coiled ceramic artificial muscles

To fabricate the homochiral coiled $Cu@Al_2O_3$ artificial muscles, an 8-ply yarn with a homochiral Archimede structure was soaked in a paraffin solution at 80°C to infiltrate the paraffin. After fixing both ends of the 8-ply yarn containing paraffin and hanging the weight, the yarn could be overtwisted in a temperature range from 30 to 50°C. As increasing the twist number, the 8-ply yarn shrank to an appropriate length and then could form a homochiral coiled ceramic artificial muscle (HCCAM) with a solenoid structure once the paraffin cooled into solid. It is worth noting that hanging different weights would affect the twist number for the ply yarn's topology transformation. Figure 4a shows a schematic diagram of using thermal to actuate the HCCAM. To maintain the stability of the solenoid structure, the HCCAM should be trained several times to remove the excessive paraffin on the surface (**Fig. S27**). It was crucial to control the temperature during training, as high temperatures would cause the paraffin to melt rapidly and then transformed the coiled structure into a DNA supercoiled structure (**Fig. S28**), which was different from other polymer artificial muscles during actuation.

As shown in Fig. 4b, the transformation of the yarn structure is due to the torque concentration, which could be regulated with the help of the viscous flow field of paraffin, and the yarn could form a solenoid structure. At the same time, the topology of the yarn changed when the viscous flow field changed. When the temperature was below 80°C, the topology of HCCAM was stable since the tensile strain within this temperature was mainly caused by the volume expansion of paraffin. When the temperature was above 80°C, the topology of the HCCAM changed to a DNA supercoiled structure after undergoing a chaotic structure, which was caused by the low thermal conductivity of paraffin wax (0.5 W/(m·K)). As a comparison, Cu has a high thermal conductivity of 401 W/(m·K). On the other hand, a slow increase in the temperature could melt the outer paraffin to drive the HCCAM, while the interior paraffin still showed a highly viscous flow state to maintain the stability of the HCCAM topology. Therefore, the HCCAM exhibited long-term cycling stability under various actuation stresses (**Fig. S29**).

Figure 4c shows the tensile actuation changes and the topology changes of HCCAM along with the heating temperature. The tensile actuation rapidly increased below 80°C, at which the topology of HCCAM was mainly a coiled structure. From 80−110°C, the HCCAM topology was chaotic that combined the coiled and DNA supercoiled structures. From 110−210°C, the HCCAM showed a DNA supercoiled structure, and its tensile actuation grew slowly. In addition, the HCCAM retained nearly 10% of actuation tensile under the actuation stress of 483.5 MPa. Figure 4d shows that the HCCAM had an energy density up to 9.85 J/g under mass normalization. In addition, the volumetrically normalized energy density of the artificial muscle was close to 10,000 KJ/m^3 (**Fig. S30**). The average power of multiple actuation cycles of the artificial muscles under different actuation stresses was shown in **Fig. S31**. When the actuation stress

was smaller, the output power was more stable. This phenomenon arose from the fact that greater actuation stress was generated by greater torque energy, which required more paraffin to stabilize the HCCAM topology. By approximating the average power of artificial muscles every two seconds to instantaneous power, the powerful output power of the Cu@Al$_2$O$_3$ ceramic yarns under a strong torque energy could be obtained more intuitively (Fig. 4e). The instantaneous output power reached 0.92 W/g, which was 2.85 times the peak output of mammalian skeletal muscle (0.323 W/g). In addition, the HCCAM also achieved 10,000 stable actuation cycles under a high actuation stress of 96.7 MPa (Fig. 4f).

On the other hand, the high conductivity of the Cu@Al$_2$O$_3$ filament yarn allowed HCCAM to be electrically driven. As shown in **Fig. S32**, the temperature of the filament yarn could reach 96°C under a voltage of 1.5 V, which could actuate the ceramic artificial muscle. If the applied voltage was < 5 V, the temperature of the yarn would not exceed 900°C. By adjusting the applied voltages, the electrical actuation performance of HCCAM was obtained. **Fig. S33** shows the tensile actuations of HCCAM at different voltages. As the voltage increased, the time to reach the same tensile actuation was shorter. The HCCAM at 5 V produced a 4.5% tensile actuation in just 2 seconds, which was 1/14 of the time taken at 1.5 V. The large input power allowed the HCCAM to produce large tensile actuation in a short time, so an overload voltage of 10 V was added to explore the output power of the HCCAM (**Video S2**). **Fig. S34** shows the average power of HCCAM during one actuation cycle and the instantaneous power per 1% tensile actuation. Within the safe voltage, the average power was close to the output power of the heat driven HCCAM. However, the overload voltage significantly boosted the instantaneous power of the HCCAM, allowing it to produce a very high power of 10.3 W/g, which was even higher than that of modern jets. The nonlinear fitting was used for the maximum output power of the ceramic artificial muscles at different voltages, and the fitting function was an exponential function, $Q = \frac{U^2}{R} t$ (Fig. 4g). It was found that the ceramic muscles always maintained a high energy conversion efficiency of > 2% by calculating the ratio between the input and output energy (**Fig. S35**). The maximum energy conversion efficiencies per 1% actuated stroke at different voltages were extracted, and the highest peak was 7.59%, which was much larger than other heat-driven artificial muscles including carbon yarns (maximum ~ 1%) (Fig. 4h).

Discussion

In this work, we solved the problem that ceramic yarns could not be twisted, and realized the synchronous enhancement of actuation stress, energy density, power density and energy conversion efficiency of oxide ceramic artificial muscles. The powerful actuation performance of artificial muscles is generally believed from the changes of twisted torque energy during the topological transformation.[30, 31] For example, twisting polymer yarns generates torque energy, and the yarn can form a coiled muscle when enough twists are inserted.[32, 33] When the artificial muscles are stimulated, the increased internal stress results in radial expansion of the yarn volume and axial contraction.[34, 35] Due to the spiral structure, the axial shrinkage increases the yarn twist and generates more torque energy to balance the internal stress.[36, 37] However, ceramic yarns with strong covalent or ionic bonds show high modulus.[38] Unlike polymer yarns that can adsorb part of the torque energy by rearranging the chain segments when being twisted, ceramic

yarns with low dislocation density are hard to adsorb torque energy by the displacement of crystals.[39] Therefore, the high-modulus ceramic filament can use almost 100% of the torque energy, so that ceramic artificial muscles have high energy density and actuation stress.

However, the high modulus makes ceramic filaments tend to form DNA supercoiled structure during twisting. A viscous flow field was thus applied to assist the ceramic filament yarns to form coiled structures. Under the action of the viscous flow field, the ceramic filament yarn was subjected to viscous resistance during the transformation of the DNA supercoiled structure, which was opposite to the torque force. Therefore, ceramic filament yarns with high torque energy formed a new steady-state coiled structure under the balance of topological energy and viscous field energy. Coiled structure relied on the action of the viscous field, so the ceramic artificial muscle would transition to the DNA supercoiled structure when the viscous flow field energy decreased. In addition, this topological transformation relied on the change of paraffin viscosity rather than volume expansion. The reduction of the viscous flow field energy could automatically convert the topological energy into a large amount of torque energy, which enabled ceramic artificial muscles with greater power and energy conversion efficiency.

In addition, oxide ceramic filament yarns are usually brittle and easily destroyed by torque energy. Since the torque force of twisted yarn was mainly concentrated on the filament surface and rapidly decreased as it penetrated deep into the filament, the increase in the shear-ability of the filament yarn was achieved by metallizing the Al_2O_3 surface, so that the prepared cermet could be subjected to torque stress under high twist. Cu has been widely used for surface metallization, but the wettability of Cu and ceramic has been an open challenge, and the fragile interface is prone to stress concentration. Industrially, cermet Cu-Al_2O_3 was prepared by sintering in an inert gas containing a certain amount of oxygen. The high temperature made Cu and Al_2O_3 form a eutectic liquid wetting interface to achieve the initial connection, and Cu/CuO were precipitated to achieve a close connection after cooling. However, since the melting point of Al_2O_3 is 2054°C, the eutectic liquid phase formation temperature usually was > 1800°C. In contrast, a composite interface layer was formed at 900°C in this study. The nano-Cu grown in the early stage of chemical plating had a diameter of ~ 10 nm, which had strong chemical activity and was easy to react with dissolved oxygen in solution to generate CuO (**Fig. S36**). Therefore, the surface metallization of Al_2O_3 by chemical plating naturally had an interface layer of Cu and CuO. In addition, the lattice spacing of α-Al_2O_3 is 0.475 nm, which is greater than the Al atomic diameter (0.182 nm) and Cu atomic diameter (0.128 nm), so it is logical for Cu atoms to invade Al_2O_3 crystals to form lattice distortion connection interface. Finally, the proposed surface modification enabled massive production of Cu@Al_2O_3 filament yarns. Dopamine is suitable for various surface modifications, but existing dopamine research rarely focuses on the field of high temperatures. In this study, dopamine was used to bond Cu and Al_2O_3 at room temperature, and then the effect of dopamine on bonding Cu and Al_2O_3 at high temperature was explored. The transformation into carbides at 300°C of dopamine could improve the wettability of the Al_2O_3 to Cu, thereby providing a basis for the subsequent bonding of cermet at 900°C.

In summary, we proposed a strategy to improve the stretchability and shear-ability of Al_2O_3 filament yarns to fabricate high-modulus homochiral ceramic artificial muscle. With the help of the dopamine layer, the chemical deposition of Cu on the Al_2O_3 filament yarn was well realized. The tight connection between Cu and Al_2O_3 and the densification of the Cu layer are realized through sintering at 900°C. The densification Cu layer and ceramic-metal interface improve the shear-ability of the ceramic filament yarn, so that it can be twisted to form an Archimedean spiral structure. After the addition of paraffin, the fabrication of homochiral ceramic artificial muscle could be realized by regulating the paraffin viscosity. The as-fabricated homochiral ceramic artificial muscle had a tensile actuating of up to 13.5%, an actuating stress of 483.5 MPa, and an energy density of 9.8 J/g. Driven by electric heat, the power output of up to 10.3 W is 18 times that of human muscle contraction, and its 7% energy conversion efficiency far exceeds other artificial muscles.

Data availability

The experimental data that support the findings of this study are available from the corresponding author upon reasonable request.

Declarations

Acknowledgement

Author contributions

J. Yan conceived and designed the project. J. Wu conducted the experimental and materials characterizations. J. Yan. and J. Wu wrote this paper and all authors contributed to discussing and revising the paper.

Competing interests

The authors declare no competing interests.

References

1.   Goto, M., Kawai, M., Nakata, M., Itamoto, K., Miyata, H., Ikebe, Y. et al. Distribution of muscle fibers in skeletal muscles of the cheetah (Acinonyx jubatus). *Mamm. Biol.* **78**, 127-133 (2013).

2.	Wilson, A., Hubel, T., Wilshin, S., Lowe, J., Lorenc, M., Dewhirst, O. et al. Biomechanics of predator–prey arms race in lion, zebra, cheetah and impala. *Nature* **554**, 183-188 (2018).

3.	Finer, J., Simmons, R. Spudich, J. Single myosin molecule mechanics: piconewton forces and nanometre steps. *Nature* **368**, 113-119 (1994).

4.	Hawley, A., Hargreaves, M., Joyner, J. Zierath, R. Integrative biology of exercise. *Cell* **159**, 738-749 (2014).

5.	Pollard, T. Cooper, J. Actin, a central player in cell shape and movement. *Science* **326**, 1208-1212 (2009).

6.	Wang, Z., Grange, M., Wagner, T., Kho, A., Gautel, M. Raunser, S. The molecular basis for sarcomere organization in vertebrate skeletal muscle. *Cell* **184**, 2135-2150 (2021).

7.	Spinks, G., Martino, N., Naficy, S., Shepherd, D. Foroughi, J. Dual high-stroke and high−work capacity artificial muscles inspired by DNA supercoiling. *Sci. Robot.* **6**, eabf4788 (2021)

8.	Haines, C., Lima, M., Li, N., Spinks, G., Foroughi, J., Madden, J. et al. Artificial muscles from fishing line and sewing thread. *Science* **343**, 868-872 (2014).

9.	Spinks, G. Advanced actuator materials powered by biomimetic helical fiber topologies. *Adv. Mater.* **32**, 1904093 (2020).

10.	Hou, W., Wang, J. Lv, J. Bioinspired liquid crystalline spinning enables scalable fabrication of high-performing fibrous artificial muscles. *Adv. Mater.* **35**, 2211800 (2023).

11.	Sun, J., Guo, W., Mei, G., Wang, S., Wen, K., Wang, M. et al. Artificial spider silk with buckled sheath by nano-pulley combing. *Adv. Mater.* **n/a**, 2212112 (2023).

12.	Liu, Z., Fang, S., Moura, F., Ding, J., Jiang, N., Di, J. et al. Hierarchically buckled sheath-core fibers for superelastic electronics, sensors, and muscles. *Science* **349**, 400-404 (2015).

13.	Mu, J., Andrade, M., Fang, S., Wang, X., Gao, E., Li, N. et al. Sheath-run artificial muscles. *Science* **365**, 150-155 (2019).

14.	Di, J., Zhang, X., Yong, Z., Zhang, Y., Li, D., Li, R. et al. Carbon-nanotube fibers for wearable devices and smart textiles. *Adv. Mater.* **28**, 10529-10538 (2016).

15.	Mirvakili, S. Hunter, I. Artificial muscles: mechanisms, applications, and challenges. *Adv. Mater.* **30**, 1704407 (2018).

16.	Chen, S., Chen, Y., Zhao, Y., Zhang, L., Zhu, C., Zhang, Y. et al. Status and strategies for fabricating flexible oxide ceramic micro-nanofiber materials. *Mater. Today* **61**, 139-168 (2022).

17.   Zhang, Y., Liu, S., Yan, J., Zhang, X., Xia, S., Zhao, Y. et al. Superior flexibility in oxide ceramic crystal nanofibers. *Adv. Mater.* **33**, 2105011 (2021).

18.   Liu, C., Liao, Y., Jiao, W., Zhang, X., Wang, N., Yu, J. et al. High toughness combined with high strength in oxide ceramic nanofibers. *Adv. Mater.* **n/a**, 2304401 (2023)

19.   Li, Z., Cui, Z., Zhao, L., Hussain, N., Zhao, Y., Yang, C. et al. High-throughput production of kilogram-scale nanofibers by Kármán vortex solution blow spinning. *Sci. Adv.* **8**, eabn3690 (2022).

20.   Ishikawa, T., Kohtoku, Y., Kumagawa, K., Yamamura, T. Nagasawa, T. High-strength alkali-resistant sintered SiC fibre stable to 2,200 °C. *Nature* **391**, 773-775 (1998).

21.   Wu, Y., Wu, J., Zhu, C., Zhang, L. Yan, J. MXene-intercalation induced ordered brick-mortar structures of allomorph junctions for enhanced flexibility in TiO2 nanofibers and photocatalytic efficiency. *Chem. Eng. J.* **465**, 142798 (2023).

22.   Charles, N., Gazzola, M. Mahadevan, L. Topology, geometry, and mechanics of strongly stretched and twisted filaments: solenoids, plectonemes, and artificial muscle fibers. *Phys. Rev. Lett.* **123**, 208003 (2019).

23.   Ghatak, A. Mahadevan, L. Solenoids and plectonemes in stretched and twisted elastomeric filaments. *Phys. Rev. Lett.* **95**, 057801 (2005).

24.   Fthenakis, Z., Zhu, Z., Teich, D., Seifert, G. Tománek, D. Limits of mechanical energy storage and structural changes in twisted carbon nanotube ropes. *Phys. Rev. B* **88**, 245402 (2013).

25.   Li, M. Lin, X. Twin distortions of the Peierls instability. *Phys. Rev. B* **81**, 153102 (2010).

26.   Lin, X., Xia, S., Zhang, L., Zhang, Y., Sun, S., Chen, Y. et al. Fabrication of flexible mesoporous black Nb_2O_5 nanofiber films for visible-light-driven photocatalytic CO_2 reduction into CH_4. *Adv. Mater.* **34,** 2200756 (2022).

27.   Zhang, Y., Zhu, C., Zhang, L., Yan, J., Yu, J. Ding, B. Polymer nanoreactor mediated controllable synthesis of flexible semiconductor quantum dot nanofiber films. *Chem. Eng. J.* **448**, 137614 (2022).

28.   Kirchhoff, G. Ueber das Gleichgewicht und die Bewegung eines unendlich dünnen elastischen Stabes. *J. Reine. Angew. Math.* **1859**, 285-313 (1859).

29.   Marko, J. Neukirch, S. Competition between curls and plectonemes near the buckling transition of stretched supercoiled DNA. *Phys. Rev. E* **85**, 011908 (2012).

30.   Leng, X., Hu, X., Zhao, W., An, B., Zhou, X. Liu, Z. Recent advances in twisted-fiber artificial muscles. *Adv. Intell. Syst.* **3**, 2000185 (2021).

31.   Zhou, X., Fang, S., Leng, X., Liu, Z. Baughman, R. The power of fiber twist. *Acc. Chem. Res.* **54**, 2624-2636 (2021)

32.   Hu, X., Li, J., Li, S., Zhang, G., Wang, R., Liu, Z. et al. Morphology modulation of artificial muscles by thermodynamic-twist coupling. *Nat. Sci. Rev.* **10**, nwac196 (2023).

33.   Leng, X., Zhou, X., Liu, J., Xiao, Y., Sun, J., Li, Y. et al. Tuning the reversibility of hair artificial muscles by disulfide cross-linking for sensors, switches, and soft robotics. *Mater. Horiz.* **8**, 1538-1546 (2021).

34.   Leng, X., Mei, G., Zhang, G., Liu, Z. Zhou, X. Tethering of twisted-fiber artificial muscles. *Chem. Soc. Rev.* **52**, 2377-2390 (2023).

35.   Aziz, S., Naficy, S., Foroughi, J., Brown, H. Spinks, G. Twist–coil coupling fibres for high stroke tensile artificial muscles. *Sens. Actuators A.* **283**, 98-106 (2018).

36.   Tawfick, S. Tang, Y. Stronger artificial muscles, with a twist. *Science* **365**, 125-126 (2019).

37.   Phan, P., Hoang, T., Thai, M., Low, H., Lovell, N. Do, T. Twisting and braiding fluid-driven soft artificial muscle fibers for robotic applications. *Soft. Robot.* **9**, 820-836 (2021).

38.   Li, X., Zhang, Y., Zhang, L., Xia, S., Zhao, Y., Yan, J. et al. Synthesizing superior flexible oxide perovskite ceramic nanofibers by precisely controlling crystal nucleation and growth. *Small* **18**, 2106500 (2022).

39.   Wang, X., Zhang, Y., Zhao, Y., Li, G., Yan, J., Yu, J. et al. A general strategy to fabricate flexible oxide ceramic nanofibers with gradient bending-resilience properties. *Adv. Funct. Mater.* **31**, 2103989 (2021).
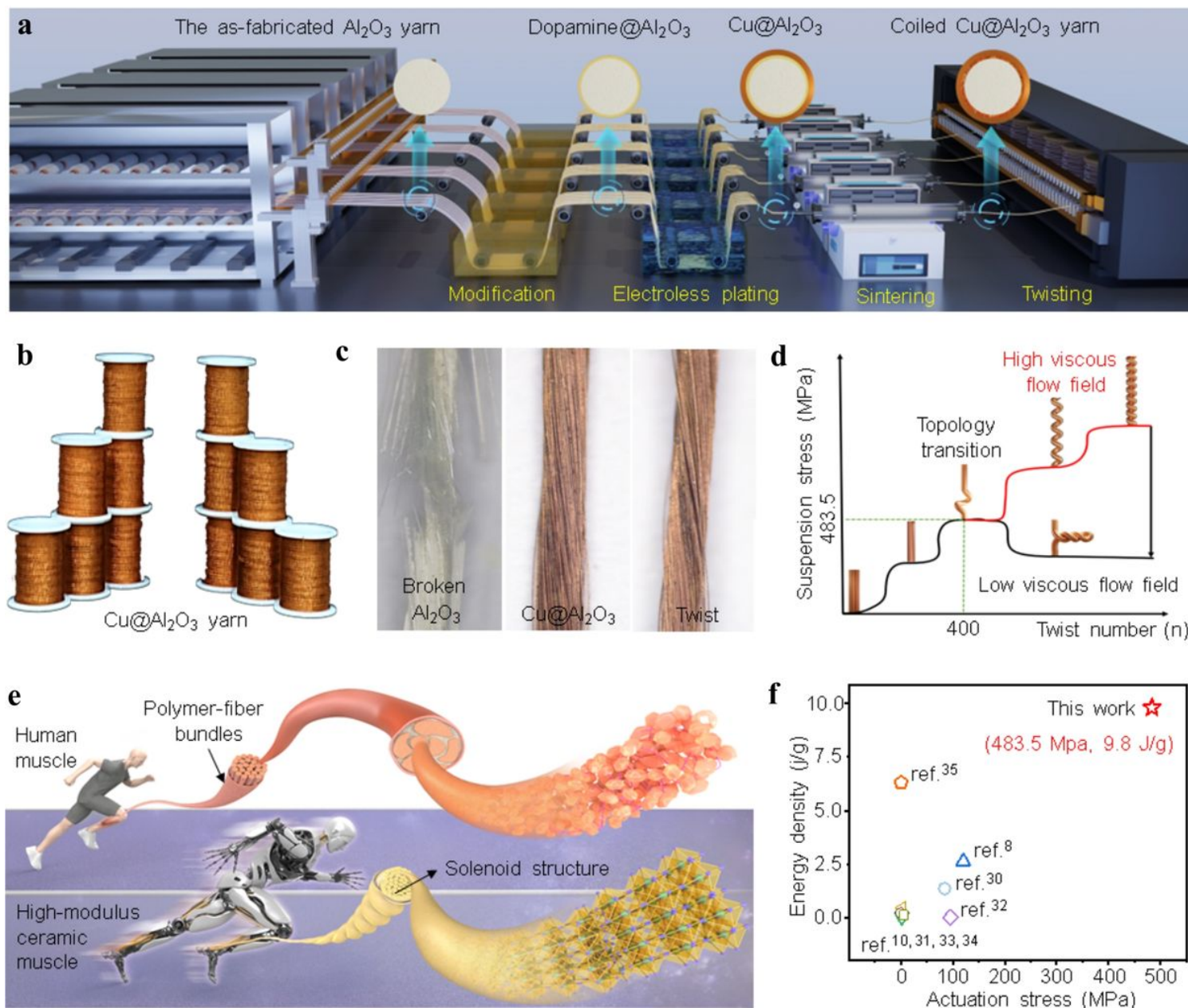
Figures

Figure 1

Large-scale fabrication of Cu@Al$_2$O$_3$ filament yarn muscles with a solenoid structure. (**a**) Schematic large-scale production of Cu@Al$_2$O$_3$ yarns in the lab. (**b**) The as fabricated rolled Cu@Al$_2$O$_3$ yarns. (**c**) Comparison of the untwisted Al$_2$O$_3$, untwisted Cu@Al$_2$O$_3$, and twisted Cu@Al$_2$O$_3$ yarns. (**d**) Topology transformation conditions for high-modulus ceramic yarns. (**e**) Conceptual diagram of the ceramic artificial muscles in comparison with human muscles. (**f**) Comparison of energy density and actuation stress of the as-fabricated Cu@Al$_2$O$_3$ artificial muscles with the reported ones.
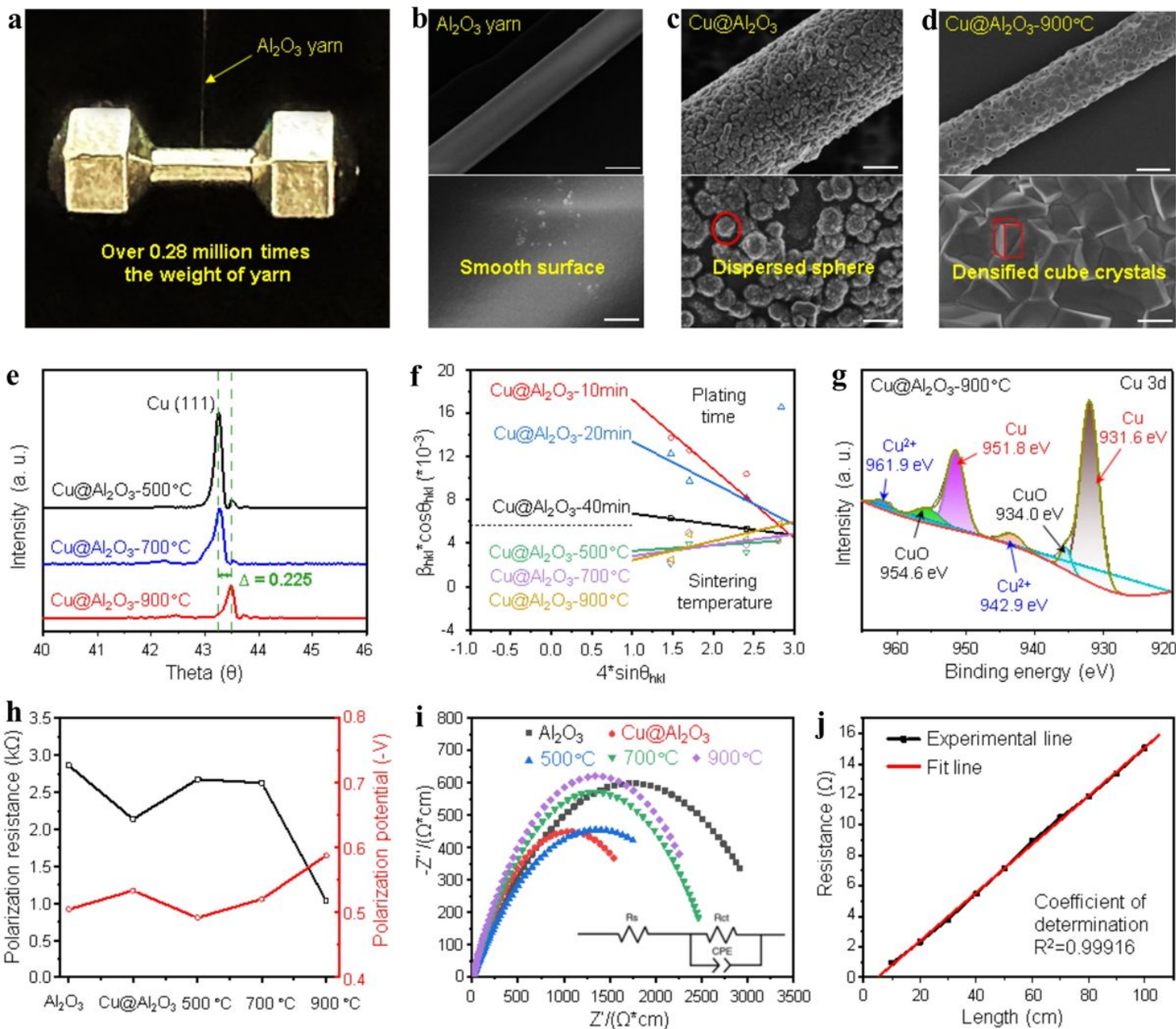
Figure 2

Materials characterization. (**a**) Demonstration of using a Al$_2$O$_3$ yarn to carry a dumbbell weighing 0.28 million times its weight. SEM images of the (**b**) bare Al$_2$O$_3$ yarn, (**c**) Cu@Al$_2$O$_3$ yarn before sintering, and (**d**) Cu@Al$_2$O$_3$-900 °C yarn sintered at 900 °C. The scale bars for the upper and bottom images are 10 μm and 1 μm, respectively. (**e**) XRD patterns of the Cu@Al$_2$O$_3$ yarns sintered at three different temperatures. (**f**) The fitting curves of Cu peak with the Williamson-Hall method. (**g**) XPS spectra of the Cu@Al$_2$O$_3$-900 °C yarn. (**h**) Polarization resistance and potential, and (**i**) EIS spectra of the bare Al$_2$O$_3$ yarn and the Cu@Al$_2$O$_3$ yarn sintered at different temperatures. (**j**) Relationship of the resistance with length of the Cu@Al$_2$O$_3$-900 °C yarn.
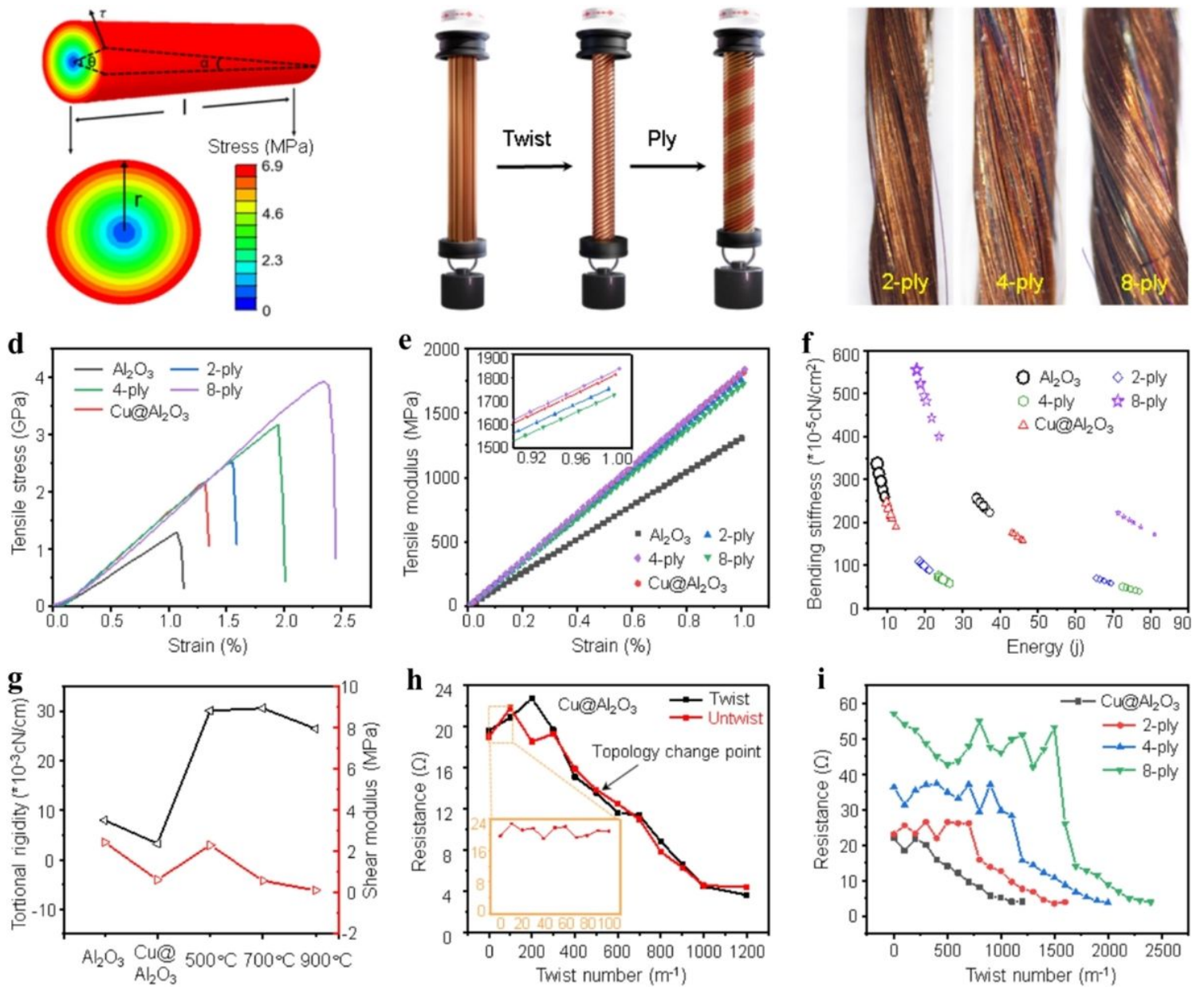
Figure 3

Mechanical and electrical properties of the homochiral torsional yarns. (**a**) Finite element analysis of ceramic yarns under a torsional stress. (**b**) Schematic diagram of forming twisted ply yarns. (**c**) Figures of the as-fabricated ply yarns of $Cu@Al_2O_3$. The tensile stress-strain curves (**d**), tensile modulus-strain curves (**e**), and bending stiffness curves (**f**) of different yarns. (**g**) The torsion rigidity and shear modulus of different yarns. (**h**) Resistance changes of the twisted and untwisted $Cu@Al_2O_3$ yarns. (**i**) Relationship between the twist number and resistance of different yarns.
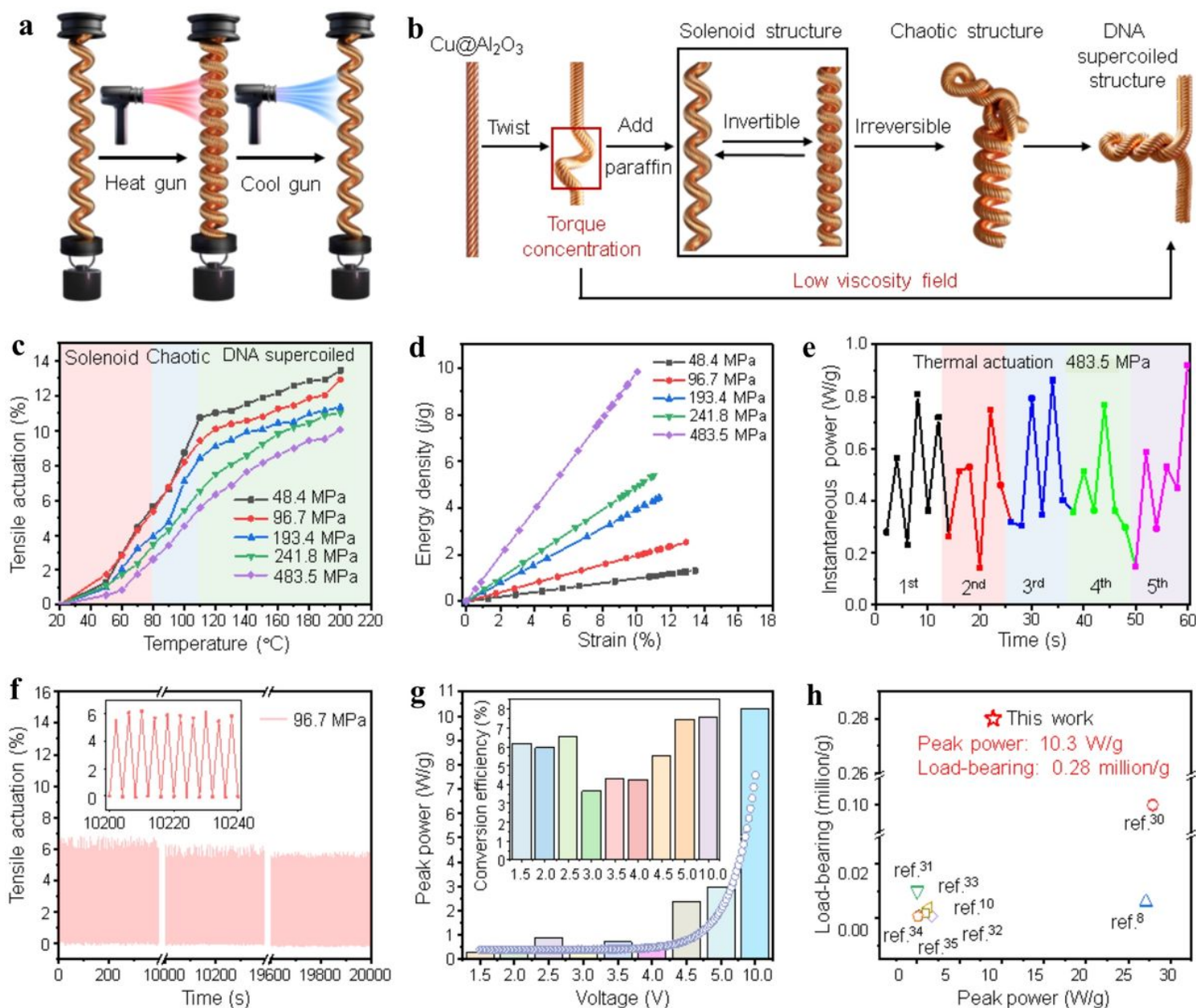
Figure 4

Actuation performance and topology transformation of the ceramic artificial muscle. (**a**) Schematic diagram of using thermal to actuate the HCCAM. (**b**) Schematic diagram of topology changes of the HCCAM. (**c**) The relationship curves between actuation strains and temperatures under different loads. (**d**) Energy density and actuation strain under different loads. (**e**) Instantaneous power of the HCCAMunder a 483.5 MPa load. (**f**) Circulatory endurance curve of HCCAMunder a 241.8 MPa load. (**g**) The peak power and peak energy conversion efficiency of the HCCAM at different voltages. (**h**) Comparison of the peak power and load bearing of HCCAM with the reported muscles.

Supplementary Files

This is a list of supplementary files associated with this preprint. Click to download.

- VideoS1.mp4
- SupplementaryInformation.docx
- VideoS2.mp4